

Procedural and learning-based generation of coral reef islands

Submission1265

Abstract

We propose a procedural method for generating single volcanic islands with coral reefs using user sketching from two projections: a top view, which defines the island's shape, and a profile view, which outlines its elevation. These projections, commonly used in geological and remote sensing domains, are complemented by a user-defined wind field, applied as a distortion field to deform the island's shape, mimicking the effects of wind and waves on the long term and enabling finer user control. We then model the growth of coral on the island and its surrounding to construct the reef following biological observations. Based on these inputs, our method generates a height field of the island. Our method is capable of creating a large variety of island models composing a dataset used for training a conditional Generative Adversarial Network (cGAN). By applying data augmentation, the cGAN allows for even greater variety in the generated islands, providing users with higher freedom and intuitive controls over the shape and structure of the final output.

1 **Keywords:** Procedural modeling, Terrain generation, cGAN,
2 Coral reef, Sketch-based interface

3 1. Introduction

4 Simulating the formation of coral reef islands presents significant
5 challenges due to the complex interplay of geological, environmental,
6 and biological factors (Hopley, 2014). One major difficulty lies
7 in capturing the long-term subsidence of volcanic islands, which
8 occurs over millions of years, while simultaneously modeling the
9 upward growth of coral reefs that rely on environmental conditions
10 such as water depth, temperature, and sunlight. This combination of
11 slow geological processes and dynamic biological growth is chal-
12 lenging to replicate in a computational model.

13 Additionally, the biological aspects of coral growth are inher-
14 ently tied to environmental factors. Coral reefs grow only within a
15 specific range of water depth and sunlight, and their growth patterns
16 are affected by the health of the reef ecosystem and the availability
17 of resources. Accurately modeling these biological dependencies in
18 a procedural system is challenging, as these factors are numerous
19 and difficult to generalize. Moreover, the scarcity of data available
20 obstructs the global understanding of these ecosystems. In a recent
21 high-resolution mapping of shallow coral reefs (Lyons et al., 2024),
22 researchers estimated the total surface area of this biome to cover
23 less than 0.7% of Earth's area, and more specifically that coral habi-
24 tat represents less than 0.2%.

25 Moreover, the need to design plausible reef structures in digi-
26 tal environments for applications such as scientific visualization,
27 simulation, or digital entertainment, calls for models that balance
28 realism with controllability. Existing terrain generation methods,
29 such as Perlin noise-based algorithms or uplift-erosion models, are
30 often ill-suited for these processes. While they can generate natural-

31 looking landscapes (such as alpine landscape, representing about a
32 quarter of land area (Körner et al., 2014)), they do not account for
33 the unique geological and biological interactions that govern coral
34 reef island formation, thus missing coherency. Capturing these dy-
35 namics, while also providing user control during the modeling of a
36 terrain, requires a balance between realism and flexibility, allowing
37 for both accurate computationally expensive simulation of natural
38 processes and intuitive user control in interactive time.

39 Despite advances in terrain generation, existing methods strug-
40 gle with user-controlled design of specific island shapes and achiev-
41 ing realism without real data. Coral reef islands exemplify this gap:
42 we lack datasets to directly train deep models, and purely procedur-
43 al methods require expert tuning to mimic their features.

44 To address these issues, we propose to use sketch-based mod-
45 eling techniques as an initial step in our approach as a means to
46 efficiently create a large and diverse set of training examples for
47 a learning-based model. Each synthetic example is represented by
48 a terrain height field and a corresponding semantic label map that
49 marks different regions, providing structured input-output pairs for
50 the learning stage.

51 We trained a conditional Generative Adversarial Network
52 (cGAN) as the core of our learning-based approach (Mirza and
53 Osindero, 2014; Isola et al., 2017). A cGAN is a type of deep learn-
54 ing model that learns to generate realistic data based on an input
55 condition or context. In our case, the cGAN takes as input the se-
56 mantic label map of an island generated by the procedural step and
57 learns to produce a realistic island height field that matches this
58 layout. By training on a large variety of examples from our curve-
59 based algorithm, the cGAN captures the subtle terrain features and
60 variations characteristic of coral reef islands, this approach sur-
61 passes the capabilities of traditional procedural rules, aided by ex-
62 ensive data augmentation. The cGAN model can be used on its

own to generate new island terrains with simplified and more intuitive user inputs through digital drawing, and the model will generate a realistic island terrain accordingly.

The key contributions are as follows: 1) a novel sketch-based procedural algorithm for shaping island terrains from top and profile views, 2) The training of a deep learning model on synthetic data derived from procedural rules, serving as an abstraction layer that hides underlying complexity, 3) A demonstration that the cGAN approach tolerates imprecise, low-detail user input sketches, broadening usability, without the need for cutting-edge network architectures, and 4) An insight that procedural generation remains essential to produce training data in data-sparse domains such as coral reef islands. These contributions collectively show a pathway to blend user-driven design with learning-based generation in terrain modeling.

2. Related work

Procedural terrain generation spans a spectrum from purely noise-driven algorithms to physics-based simulations and, more recently, data-driven methods. In the context of coral reef islands, where both long-term geological subsidence and biogenic reef accretion interplay, existing approaches fall short in one of two ways: either they lack ecological or geological grounding, or they offer insufficient authoring control.

Procedural and simulation-based methods Noise-based techniques such as Perlin noise (Perlin, 1985), Simplex noise (Perlin, 2001), and the Diamond-Square algorithm (Fournier et al., 1982) (often extended via fBm or multifractal noise (Musgrave et al., 1989; Ebert et al., 2003)) remain popular for their simplicity and speed. Island shapes are generated by modulating noise with radial falloff masks (Olsen, 2004), but these methods cannot reproduce reef rings, lagoons, or atoll structures in a geologically coherent manner. They treat terrain purely as a signal-processing problem, divorced from processes like volcanic subsidence or coral growth (Smelik et al., 2009; Galin et al., 2019).

Simulation-based approaches introduce causality by modeling erosion (Beneš et al., 2006; Neidhold et al., 2005; Mei et al., 2007), tectonic uplift (Cordonnier, Braun, et al., 2016; Cordonnier, Cani, et al., 2017; Schott et al., 2023), or vegetation-terrain feedback (Ecormier-Nocca et al., 2021; Cordonnier, Galin, et al., 2017). Hydraulic and thermal erosion capture fluvial networks and slope-driven mass wasting, but they omit underwater sedimentation and biogenic carbonate accretion. Tectonic and isostatic models excel at orogeny but ignore coral reef dynamics, while vegetation-based methods do not generalize to marine ecosystems. Consequently, none of these simulations jointly capture the slow subsidence of volcanic islands and the compensatory growth of surrounding reefs on the timescales required for atoll formation.

Sketch-based terrain modeling Sketch-driven interfaces bridge user intent and procedural detail. Curve-based systems let users draw ridges, valleys, or coastlines that guide surface deformation and noise propagation (Gain et al., 2009; Hnaidi et al., 2010). Constraint-based methods extend this by enforcing absolute elevation or slope values at control curves or points, solved via diffusion or fractal interpolation (Gasch et al., 2020; Talgorn and Belhadj,

2018), and even gradient-domain editing for slope control (Guérin, Peytavie, et al., 2022). Semantic approaches encode high-level "terrain atoms" from a dictionary of primitives (Génevaux et al., 2015) or interpret geological schematics into 3D models (Natali et al., 2012). While these techniques grant artists fine-grained control, they typically lack ecological constraints and have not been tailored to marine biogeomorphology.

Learning-based terrain synthesis Deep generative models offer a way to learn complex patterns without explicit procedural rules. Unconditional GANs have been applied to digital elevation maps of mountains (Wulff-Jensen et al., 2018) and joint height-texture synthesis (Spick and Walker, 2019), but their reliance on latent noise prevents precise layout control. Two-stage pipelines use an initial GAN for heightmaps and a conditional GAN for textures (Beckham and Pal, 2017) or reverse the order (imagery-to-DEM) (Panagiotou and Charou, 2020), yet still lack the ability to guide authoring.

Conditional GANs (cGANs) extend image-to-image translation methods such as pix2pix (Isola et al., 2017) to terrain, enabling sketch- or label-map-conditioned generation. Prior work includes sketch-to-DEM translation for generic landforms (Guérin, Digne, Galin, Peytavie, et al., 2017) and sparse "altitude dot" conditioning (Voulgaris et al., 2021), as well as cGANs that invert satellite imagery into elevation (Sisodia, 2022). However, these models require extensive paired real-world datasets which are scarce for coral reef islands.

3. Overview

Our method for procedural generation of coral reef islands is composed of two independent modeling techniques shown in Figure 1. A first algorithm, curve-based (top-left blue block, is presented in Section 4), parametrize the surface of islands by a top-view sketch interface, describing the outlines of the regions composing it and a stroke-based wind field deforming them, as well as a profile-view sketch describing for each region its altitude and resistance to deformations. User inputs are given as 1D functions (altitude and resistance), a 1D polar function (island outlines) and a 2D vector field (wind field) as shown in Figure 2, which are convenient to randomize through the use of noise, but hindering users' modeling freedom.

On the other hand, we include a second generation algorithm, learning-based (right red blocks from the pipeline figure, developed in Section 6), which train a neural generator G to transform a labeled image into a height field. Parallelly, a discriminator D is trained to distinguish height fields provided from the training set against height fields generated by G . This adversarial training strengthens the outputs of the generator, up to the point where we discard the discriminator and training data, only keeping the generation step (bottom-right). Users are then able to provide unseen label maps and obtain height fields as close as possible to the training dataset. This method for terrain modeling is poorly constrained, however requires a large amount of prior data in its training set, which are not available in our case.

We connect these two algorithms through a process of dataset generation (central orange block, described in Section 5) in order to enforce the benefits of each while reducing their limitations. Given the initial curve-based user inputs, we create a dataset composed of

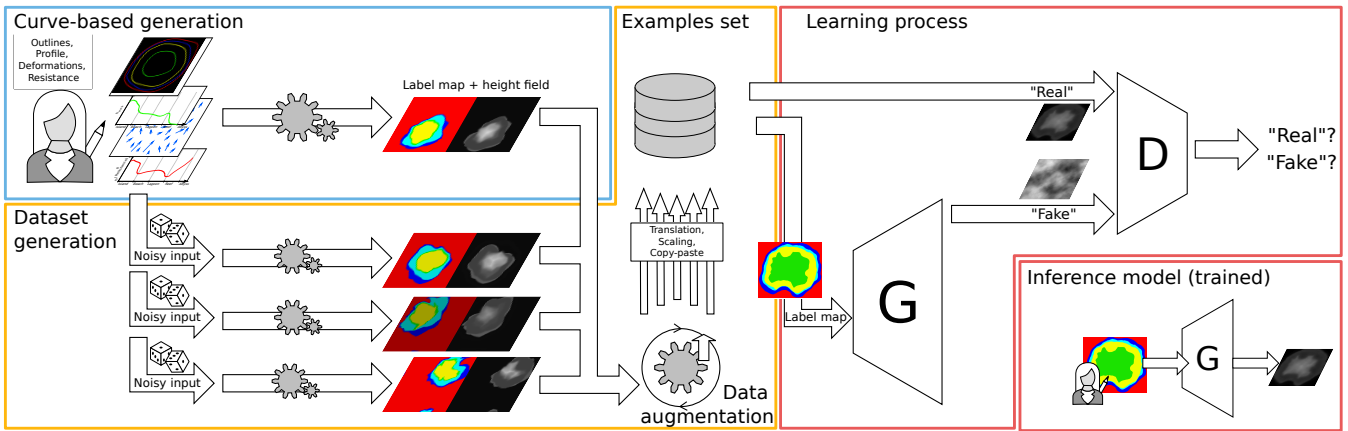


Figure 1: Our pipeline first prompt our user to create single pairs of coral reef islands' height fields and label maps using our proposed curve-based modeling algorithm (Section 4). The same algorithm is applied multiple times on randomly altered versions of the user input to create a dataset, which we further enhance with data augmentation techniques Section 5. Finally, we train a conditional Generative Adversarial Network which can then be used standalone to create height fields from labeled sketches (Section 6).

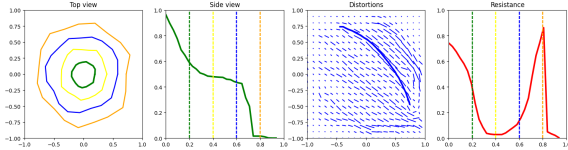


Figure 2: The user can interact directly on the island by editing the different canvases in no specific order. This UI shows, from left to right, the top-view sketch with the different outlines of each regions, the profile-view sketch with the outlines represented in dotted lines, the wind velocity sketch drawn with strokes (last stroke is visible), and the resistance function showing here a high resistance at the top of the island and on the front reef.

188 two intuitive sketch-based inputs from the user: a top-view sketch
 189 and a profile-view sketch, which define the islands horizontal lay-
 190 out and vertical elevation profile. In addition to these sketches, the
 191 user can further refine the terrain by applying wind deforma-
 192 tion strokes, which simulate the effects of wind and waves on the is-
 193 lands shape. This combination of sketches and wind inputs gives
 194 users precise control over both the islands structure and its natural
 195 variations, such as irregular coastlines or concave features. We will
 196 present the usefulness of these sketches in this section, and describe
 197 the technical details in the next section.

198 4.1. Initial height field generation

199 The top-view sketch defines the island's outline as seen above.
 200 Using a simple drawing interface, the user delineates concentric
 201 boundaries for key regions such as the island itself, the beaches, the
 202 lagoon, and the surrounding abyss, around the canvas center. Each
 203 boundary is represented in polar coordinates, where r_p is the radial
 204 distance from the island's center and θ_p is the angular position.
 205 Allowing r to vary with θ introduces irregular, natural shapes rather
 206 than perfect circles (Figure 3).

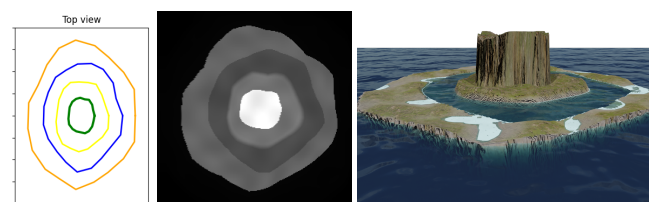


Figure 3: Using only the outlines from the top-view sketch, each point in the field is assigned a region (island, beach, lagoon, abyss), which later guides its height assignment.

171

172

173

174

175

176

177

178

179

180

181

182

183

184

185

186

187

188

189

190

191

192

193

194

195

196

197

198

199

200

201

202

203

204

205

206

207

208

209

210

211

212

213

214

215

216

217

218

219

220

221

222

223

224

225

226

227

228

229

230

231

232

233

234

235

236

237

238

239

240

241

242

243

244

245

246

247

248

249

250

251

252

253

254

255

256

257

258

259

260

261

262

263

264

265

266

267

268

269

270

271

272

273

274

275

276

277

278

279

280

281

282

283

284

285

286

287

288

289

290

291

292

293

294

295

296

297

298

299

300

301

302

303

304

305

306

307

308

309

310

311

312

313

314

315

316

317

318

319

320

321

322

323

324

325

326

327

328

329

330

331

332

333

334

335

336

337

338

339

340

341

342

343

344

345

346

347

348

349

350

351

352

353

354

355

356

357

358

359

360

361

362

363

364

365

366

367

368

369

370

371

372

373

374

375

376

377

378

379

380

381

382

383

384

385

386

387

388

389

390

391

392

393

394

395

396

397

398

399

400

401

402

403

404

405

406

407

408

409

410

411

412

413

414

415

416

417

418

419

420

421

422

423

424

The profile-view sketch defines the island's vertical elevation along any radial direction. Here, the user draws a curve that specifies height at key terrain milestones, such as the central peak, island border, beach, lagoon, and abyss, creating a continuous 1D height function $h_{\text{profile}}(\tilde{x})$ where \tilde{x} is a parametric distance measuring position along the sequence of regions. This continuous profile ensures smooth elevation transitions across all terrain features.

By combining the top-view and profile-view sketches via revolution modeling, the system generates a full 3D terrain model that matches the user's design. The process begins by transforming those two sketches into a coherent height field (Figure 5).

For any point \mathbf{p} on the terrain, the system computes polar coordinates $(r_{\mathbf{p}}, \theta_{\mathbf{p}})$. The radial distance $r_{\mathbf{p}}$ determines which region the point belongs to (island, beach, lagoon, reef, or abyss) based on the user-defined radial limits. Those outlines from the top-view sketch provide the exact boundaries between regions.

Each point's height is computed using the profile function $h_{\text{profile}}(\tilde{x})$. Instead of using the raw radial distance $r_{\mathbf{p}}$, we define a parametric region distance $\tilde{x}_{\mathbf{p}}$ that maps each point to a normalized position along the concentric regions (see Figure 4). The radial space is divided by user-defined boundaries R_0, R_1, \dots, R_n , corresponding to the island center, border, beach, lagoon, and abyss.

When a point \mathbf{p} lies between two boundaries, say R_i and R_{i+1} , its parametric distance is

$$\tilde{x}_{\mathbf{p}} = i + \frac{r_{\mathbf{p}} - R_i}{R_{i+1} - R_i}, \quad (1)$$

where i is the index of the region containing \mathbf{p} (i.e., $R_i \leq r_{\mathbf{p}} < R_{i+1}$). This linear mapping stretches each region's radial span to the interval $[i, i+1]$, ensuring smooth interpolation across region boundaries. The final height at point \mathbf{p} is then

$$h(\mathbf{p}) = h_{\text{profile}}(\tilde{x}_{\mathbf{p}}). \quad (2)$$

4.1.1. Wind deformation

To break the radial symmetry inherent in sketch-based terrain generation and introduce more organic island shapes, we allow the user to define a wind velocity field via freehand strokes on a 2D canvas. Each stroke is represented as a parametric curve C , interpreted as a local wind flow with direction C' , strength S , and influence width σ . These strokes simulate wind and wave erosion effects on the terrain.

The deformation vector at any terrain point \mathbf{p} is computed as a sum over all strokes, weighted by a Gaussian falloff centered on the closest point \mathbf{p}_C^* along each curve (Figure 6, top):

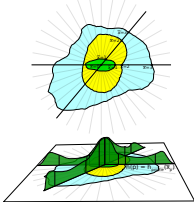


Figure 4: Parametric distance \tilde{x} depending on angle θ .

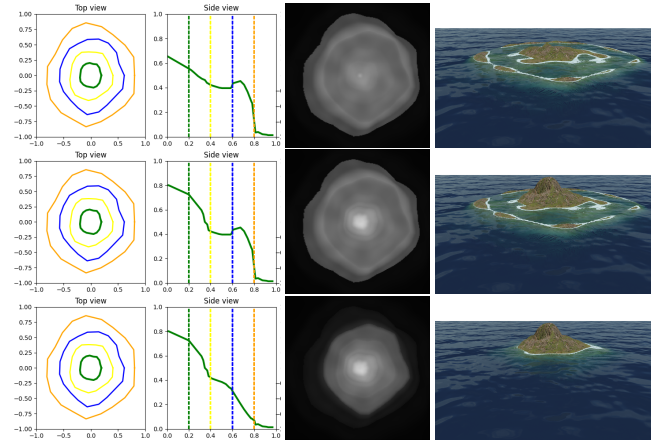


Figure 5: Providing a smooth function between each region results in islands with plausible reliefs. We fixed the outlines while editing only the height function in order to produce, from top to bottom, a low island, a coral reef island, and finally an identical island without the reef.

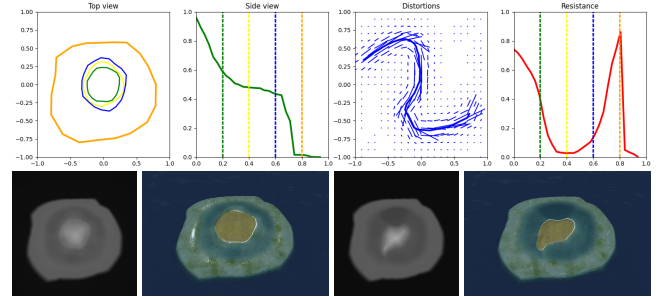


Figure 6: Defining a top-view wind vector field from user-provided strokes (top, blue) in association with a resistance function (top, red), a height field is deformed accordingly. Right: original height field and render; Left: altered results. The beach and lagoon regions are defined with low resistance, which is visible by having only these regions deformed in bottom results.

$$\Phi(\mathbf{p}) = \sum_{C \in \text{curves}} S \frac{C'(\mathbf{q})}{\|C'(\mathbf{q})\|} \cdot G_{\sigma}(\|\mathbf{p} - \mathbf{p}_C^*\|) \quad (3)$$

$$G_{\sigma}(x) = \frac{1}{\sigma\sqrt{2\pi}} e^{-\frac{x^2}{2\sigma^2}}. \quad (4)$$

To preserve semantic structure across terrain regions, a resistance function $\rho(\tilde{x})$ modulates the deformation based on terrain zones such as beach, lagoon, or abyss (Figure 7). The final deformation vector becomes:

$$\tilde{\Phi}(\mathbf{p}) = (1 - \rho(\tilde{x}_{\mathbf{p}})) \cdot \Phi(\mathbf{p}). \quad (5)$$

256 This warp is applied to both the height field and the label map,
 257 ensuring consistent semantic deformation. For example, applying
 258 strokes to one side of a circular island creates concave coastlines
 259 while leaving high-resistance regions (e.g., the abyss) unaffected,
 260 simulating the localized impact of natural erosion (Figure 6, bot-
 261 tom).

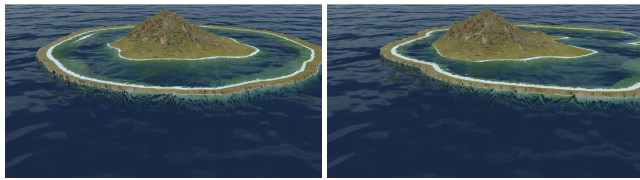


Figure 7: (Left) An island defined with a high resistance, under a uniform lateral wind velocity field, and (right) the same island with lower resistance on the reef borders, simulating the effect of coastal erosion.

262 4.2. Coral reef modeling

263 Once the terrain has been generated and deformed by the wind, we
 264 simulate the long-term geological evolution of coral reef islands
 265 through two parallel processes: the subsidence of the volcanic is-
 266 land and the upward growth of coral reefs. As observed in nature,
 267 the volcanic base sinks over time while coral formations grow ver-
 268 tically to remain close to the water surface, following the "keep-up"
 269 strategy of reef development.

270 4.2.1. Subsidence

271 Subsidence is modeled by uniformly scaling the original terrain
 272 height downward, simulating the gradual sinking of the volcanic
 273 landmass due to tectonic processes. The user specifies a subsidence
 274 rate $\lambda \in [0, 1]$, which controls how much the island has sunk. The
 275 subsided terrain is computed as:

$$h_{\text{subsid}}(\mathbf{p}) = (1 - \lambda) \cdot h_0(\mathbf{p}) \quad (6)$$

276 This factor is applied uniformly across the island, offering a geo-
 277 logically plausible and computationally efficient approximation of
 278 large-scale subsidence.

279 4.2.2. Coral reef growth

280 Coral reef growth is modeled independently from the subsiding ter-
 281 rain. The system generates a coral-specific height field $h_{\text{coral}}(\mathbf{p})$
 282 that remains near the sea surface regardless of the island's verti-
 283 cal shift, reflecting coral growth in biologically viable depth ranges
 284 (typically 0-30 meters below sea level).

285 We define distinct reef zones anchored at specific depths:

- 286 • Reef crest near sea level: $h_{\text{crest}} = -2 \text{ m}$
- 287 • Back reef and lagoon: $h_{\text{back}} = -20 \text{ m}$
- 288 • Fore reef sloping to abyss: $h_{\text{abyss}} = -100 \text{ m}$

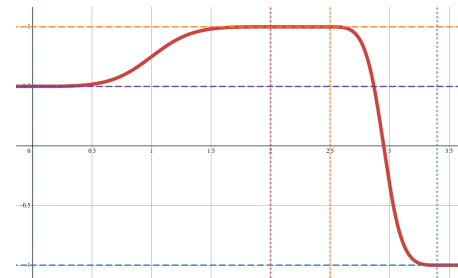


Figure 8: The modeling of the reef growth in our model is described by a piecewise function h_{coral} which is flat in the lagoon, the crest and abyss, and follows a smoothstep function as transitions for the backreef and fore reef regions. Zones' anchor heights are represented by horizontal dashed lines; zones' limits are dotted vertical lines.

289 Each reef subregion is defined over a parametric domain $x \in$
 290 $[0, 1]$, with $x = 0$ the begining of the reef region and $x = 1$ its end,
 291 directly inputting the parametric distance $x = \tilde{x} - i_{\text{reef region}}$. For in-
 292 stance:

- 293 • Back reef: $x_{\text{back,start}} = 0, x_{\text{back,end}} = 0.5$
- 294 • Reef crest: $x_{\text{crest,start}} = 0.75, x_{\text{crest,end}} = 0.8$
- 295 • Abyss begins at $x_{\text{abyss,start}} = 1$

296 We model transition zones between these regions using a
 297 smoothstep operator:

$$\text{smoothstep}(x) = 3x^2 - 2x^3 \quad (7)$$

298 We denote the interpolating function as:

$$S(a, b, x_0, x_1, x) = a + (b - a) \text{smoothstep}\left(\frac{x - x_0}{x_1 - x_0}\right) \quad (8)$$

299 The complete coral height field, as displayed in Figure 8, is built
 300 as a piecewise function:

$$h_{\text{coral}}(x) = \sum_{r \in \text{subregions}} \begin{cases} h_r & \text{if } x_{r,\text{start}} \leq x \leq x_{r,\text{end}} \\ 0 & \text{otherwise} \end{cases} \\ + \sum_{t \in \text{transitions}} \begin{cases} S(h_t, h_{t+1}, x_{t,\text{end}}, x_{t+1,\text{start}}, x) & \text{if } x_{t,\text{end}} < x < x_{t+1,\text{start}} \\ 0 & \text{otherwise} \end{cases} \quad (9)$$

301 4.2.3. Output

302 Finally, we merge the island base height field and the coral reef
 303 height field by our *ad-hoc* smooth maximum operator smax defined
 304 as:

$$\text{smax}(a, b) = \begin{cases} a + \frac{\delta}{2k} \left(\frac{1}{1 + e^{-k\delta}} + \frac{1}{1 - e^{-k\delta}} \right) & \text{for } a \neq b \\ a + \frac{1}{2k} & \text{for } a = b \end{cases} \quad (10)$$

305 with $\delta = b - a$ for conciseness, and k a sharpness parameter approx-
 306 imating the max operator as k grows. At $k = 5$, the operator max is

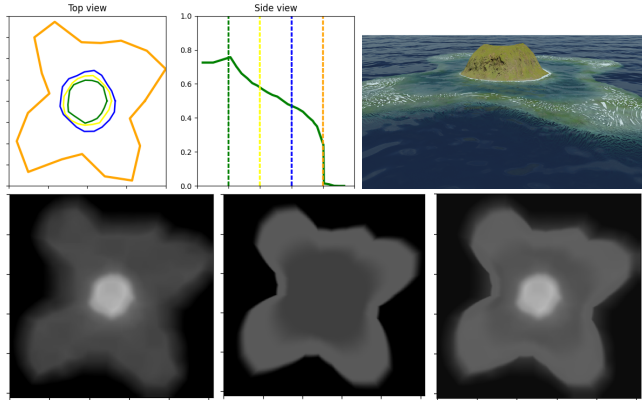


Figure 9: Volcano with single vent. (Bottom right) The initial height field is computed directly from the user input, (bottom center) the reef height field is outputted from Equation (9), and finally, (bottom left) we blend the two results with Equation (10).

already well approximated while conserving continuity in the resulting height field $\mathcal{H}(p) = \text{smax}(h_{\text{subsidi}}(\mathbf{p}), h_{\text{coral}}(\mathbf{p}))$.

The resulting terrain represents a plausible coral reef island, where the volcanic island has subsided, and coral reefs have grown upward to keep pace with the water level (Figure 9). The smooth blending between the subsided terrain and the coral features ensures a natural transition between regions like the island, lagoon, and coral reefs.

5. Data generation

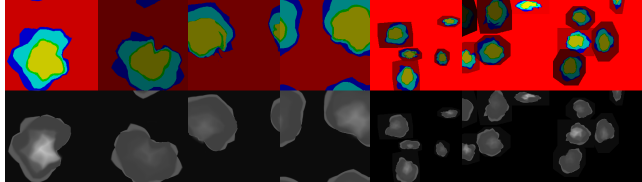


Figure 10: Examples from a dataset with increasing data augmentation.

The creation of the dataset is done through the use of the procedural curve-based modeling algorithm for which we alter the input parameters.

For each generation, the top-view and profile-view sketches use an initial layout. Each outline of the top-view sketch is defined as a centered circle of random radius $r_{\min} \leq r^* \leq r_{\max}$. We add another deformation based on fBm noise η such that the final contour, profile, and resistances, are defined as

$$\begin{aligned} r(\theta) &= r^* + \eta_{\text{contours}}(\theta) \\ h_{\text{profile}}(\tilde{x}) &= h_{\text{profile}}^*(\tilde{x}) \cdot \eta_{\text{profile}}(\tilde{x}) \\ \rho(\tilde{x}) &= \rho^*(\tilde{x}) \cdot \eta_{\text{resistance}}(\tilde{x}) \end{aligned}$$

Finally, we need to generate a random wind field. The realistic nature of wind is ignored for the generation of the wind strokes in order to provide complexity and variety in the results. We generate a random number n of strokes and their path by a uniformly sampling a random number m of points. The spread and intensity of each stroke is also random.

Once all inputs are set, we generate an example for multiple level of subsidence $\lambda \in [0, 1]$ to obtain a height field incorporating the coral reef modeling and the associated label map.

We use of the Hue component to encode the labels directly from the parametric distance $H = |\tilde{x}|$ while the subsidence rate into the Value component $V = \lambda$. Moreover, we purposefully left the Saturation component unchanged at this stage, reserving space for potentially including another parameter in the future.

Data augmentation

To enhance the variety of the dataset and improve the model's ability to generalize, we apply several data augmentation techniques in addition of the usual affine transformations (rotation, scaling, and flipping):

Translation: Since the original algorithm always centers the island, we translate the islands within the image to remove this constraint (Figure 10, leftmost). This ensures that the cGAN can generate islands in any position within the frame. By wrapping the island on the borders, the model learns that data can appear on the edges on the image.

Copy-paste: In some cases, we combine multiple islands into a single sample, with only a maximum intersection over union (IoU) of 10%, allowing the abysses to overlap but without obtaining other region types to merge. Height fields blending is done through the smooth maximum function from Equation (10), and the label blending uses the usual max operator. The regions not covered by any island are assigned the abyss ID, which is very close to the minimal height, meaning that in this case specifically, the subsidence factor (Value channel) is close to irrelevant (Figure 10, rightmost).

All augmentation techniques are applied both to the height field and the label map simultaneously to ensure consistency between the input (the label map) and the output (the height field).

6. Learning-based generation

In this section, we introduce the use of a conditional Generative Adversarial Network (cGAN), specifically the pix2pix model proposed by Isola et al., 2017, to enhance the island generation process by increasing the variety and flexibility of terrains. While the curve-based modeling algorithm can create numerous island examples, cGAN provides additional flexibility in generating more complex terrain without the rigid constraints of the curve-based algorithm that stem from our initial assumptions based on coral reef formation theory.

The training was performed using a batch size of 1, and optimized using the Adam optimizer with a learning rate of 0.0002 and momentum parameters $\beta_1 = 0.5$ and $\beta_2 = 0.999$. The loss function

375 combined a conditional adversarial loss and an L1 loss, where the
 376 L1 loss was weighted by a factor $\lambda = 100$. The generator follows
 377 a U-Net architecture with encoder-decoder layers and skip connec-
 378 tions, while the discriminator was based on a PatchGAN, classi-
 379 fying local image patches. These parameters are directly used from
 380 the original paper.

381 The inference of our model, with a dataset of approximatively
 382 10 000 examples representing about 30 minutes of training, still
 383 outputs grid artifacts, visible in Figure 11. After the second epoch,
 384 visual artifacts are already rare. This training time seems long but,
 385 at the best of our knowledge, is the shortest training time for terrain
 386 generation with learning-based approach in the litterature, mostly
 387 due to the mathematical nature of our dataset.

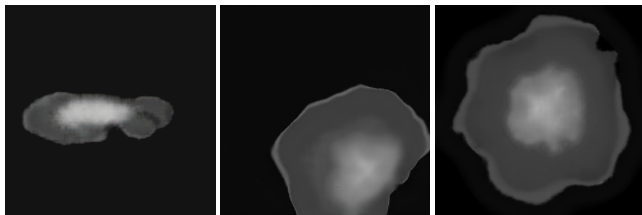


Figure 11: After the first epoch (left), grid artifacts similar to low resolution image are visible, but are being corrected during a second epoch (middle). After the second epoch, erosion patterns appear in the hieght fields (right).

388 The Python script for the initial island dataset generation is
 389 poorly optimized and takes about 2.5s per island of size 256×256
 390 as the parallelization does not take place here. Implementing an opti-
 391 mized C++ version of the initial generation process reduces this
 392 execution time to 50ms per generation.

393 On the other hand, the inference time of our deep learning model
 394 for a single input image of dimension 256×256 is constant what-
 395 ever the complexity of the scene. Using the NVIDIA GeForce GTX
 396 1650 Ti GPU with Python 3.10 and PyTorch version 2.5.1+cu121,
 397 the inference time measured is 5ms (std 1.1ms).

398 7. Results

399 The resulting model for coral island generation enables a high
 400 control-level from a user perspective as the unconstraint painting
 401 allows for complex scenarios while producing in real-time the re-
 402 sulting height fields. In this chapter we used the software Blender
 403 to provide renders directly from the outputted height fields. As our
 404 pix2pix model is trained to output 256×256 images, the resolution
 405 of the 3D models is limited by this architecture.

406 Using deep-learning-based models, most constraints from our
 407 initial assumptions are lifted (radial layout, isolated islands, ...).
 408 The control over the overall shapes of the islands regions are given
 409 through digital painting, here using the GIMP software. Each pixel
 410 of the image are encoded in HSV, with the region identifier encoded
 411 in the Hue channel. The user may increase or decrease the subsi-
 412 dence level of the island by modifying the Saturation channel over
 413 the whole image (see Figure 12).

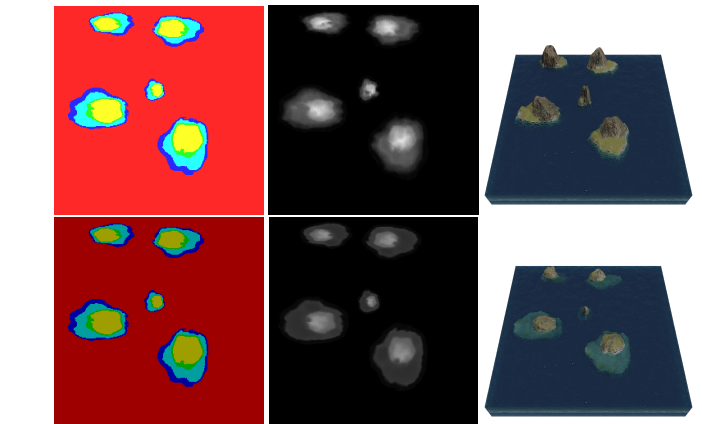


Figure 12: An identical label map yield similar height fields over multiple inferences from the model, even after modifying the subsidence factor (visible in the luminosity of the input image).

414 Since the model is based on statistics over the pixel values in-
 415 stead of hard values, users are not limited to a finite number of
 416 region identifiers, meaning that the output is more or less robust to
 417 noise (due to image compression, for example) and to the fuzzy val-
 418 ues resulting from anti-aliasing of brushes often set by default, or
 419 resizing algorithm, by image editors, or even due to compression
 420 algorithm. The example displayed in Figure 13 presents a sketch
 421 for which the outlines of the regions are at the same time blurry
 422 and with layouts that are not expected (such as the small red re-
 423 gions inside the southern lagoon region or the adjacency of beach
 424 regions directly with the abyssal region) on the top figure and over-
 425 saturated on the bottom figure. The learned model does not include
 426 inconsistancies and results in plausible 3D models. We can note
 427 that the input label map doesn't require to be hand drawn, as a sim-
 428 ple Perlin noise can produce it randomly, as shown in the examples
 429 of Figure 16.

430 The tolerance over the input values may be used to provide even
 431 more control about the transitions between two regions. Figure 14
 432 shows an example of input map with regions that are leaking over
 433 neighboring regions, and the introduction of new hue values non-
 434 existant in the dataset (light green and dark green) but are the inter-
 435 polated hue value of mountain regions and beach regions.

436 Since the curve-based procedural phase included low random-
 437 ness, the output of the cGAN is limiting its unpredictability and the
 438 results to a slight change on the input create only slight changes on
 439 the output, preventing unexpected results. Figure 12 shows the
 440 result of an input map with only a variation on the subsidence level,
 441 the resulting height fields are very similar. Adding the real-time
 442 computation of outputs, it becomes possible to construct progres-
 443 sively a landscape and correct small mistakes to intuitively design
 444 islands inspired by real-world regions. A creation of an island simi-
 445 lar to Mayotte, presented in Figure 15 was hand-made in few min-
 446utes.

Limitations While this approach brings significant advantages,
 there are also some limitations to consider. The reliance on a syn-

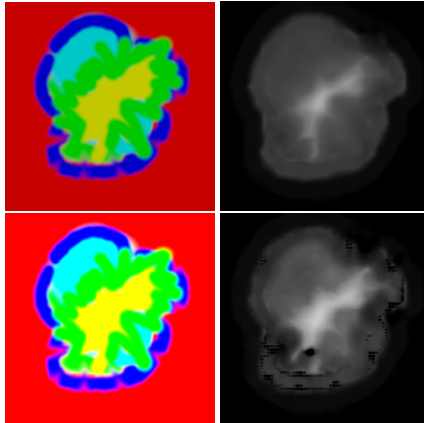


Figure 13: User applied fuzzy brushes to draw the label map, resulting in some pixels that are inconsistent with the dataset and unlogical island layouts: abyss regions (red) are found between beach (green), lagoon (cyan) and reef regions (blue). The neural model ignores the layout inconsistencies, and partially over-saturation as long as the pixel isn't completely white.

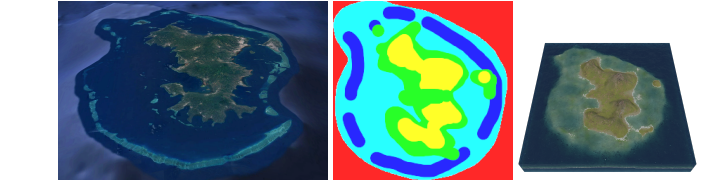


Figure 15: Comparison between of real (left, from Google Earth) and synthetic (right) islands of Mayotte. The label map (center) is hand drawn to match approximatively its real-world counterpart.

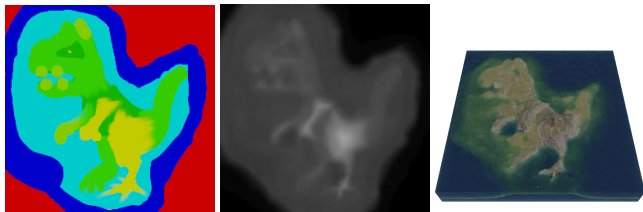


Figure 14: Without constraints on the generation, the user may use unrealistic layout and the neural network will however output a plausible result. Here new colors have been added (pistachio), but the network naturally considers it as a transition from mountain to beach.

466 system. Many other neural networks models could be exploited to
 467 increase the possibilities, such as newer variants of cGANs (Park
 468 et al., 2019), or models with style transfer functionalities (Gatys
 469 et al., 2015; Zhu et al., 2020) in order to change the overall aspect
 470 of a terrain (Perche et al., 2023b, 2023a), use text-to-images mod-
 471 els (Rombach et al., 2021; Radford et al., 2021) to generate height
 472 fields from a verbal prompt, or super-resolution models (Dong
 473 et al., 2014) to increase the definition of details in the final output
 474 (Guérin, Digne, Galin, and Peytavie, 2016).

475 8. Conclusion and future work

476 This work has presented a novel approach to generating coral reef
 477 island terrains by combining traditional procedural methods with
 478 deep learning techniques. We first developed a procedural gener-
 479 ation algorithm capable of creating a wide variety of island terrains
 480 through a combination of top-view and profile-view sketches, wind
 481 deformation, and subsidence and coral reef growth simulation. By
 482 applying these methods, we were able to produce realistic terrains
 483 based on geological processes, capturing key features of coral reef
 484 islands such as beaches, lagoons, and coral reefs.

485 To further enhance flexibility and realism in the generation pro-
 486 cess, we incorporated a conditional Generative Adversarial Net-
 487 work (cGAN), using the pix2pix model to generate height maps
 488 from label maps of island features. The cGAN model allowed us to
 489 overcome some of the constraints inherent in the procedural algo-
 490 rithm, such as radial symmetry and fixed island positioning. With
 491 data augmentation techniques, we were able to train the cGAN on
 492 a synthetic dataset, generating varied and realistic island terrains.

493 References

- 494 Beckham, C., & Pal, C. (2017). A step towards procedural terrain
 495 generation with gans. <http://arxiv.org/abs/1707.03383>
 496 (cit. on p. 2).
- 497 Beneš, B., Těšínský, V., Hornyš, J., & Bhatia, S. K. (2006). Hy-
 498 draulic erosion. *Computer Animation and Virtual Worlds*,
 499 17, 99–108. <https://doi.org/10.1002/cav.77> (cit. on p. 2).
- 500 Cordonnier, G., Braun, J., Cani, M.-P., Benes, B., Galin, É., Pey-
 501 tavie, A., & Guérin, É. (2016). Large scale terrain genera-
 502 tion from tectonic uplift and fluvial erosion. *Computer
 503 Graphics Forum*, 35, 165–175. <https://doi.org/10.1111/cgf.12820> (cit. on p. 2).

449 synthetic dataset means that the cGAN inherits some biases and lim-
 450 itations of our initial curve-based algorithm. This could limit
 451 the true diversity of the terrains that the model can generate, as the
 452 output is confined by the patterns present in the training data. Addi-
 453 tionally, the cGAN model's internal logic lacks transparency, offer-
 454 ing limited user control over the generation process once the model
 455 has been trained. Moreover the training time is far from real-time.

456 **Future work** Further improvements could be made to the synthetic
 457 dataset. Incorporating more complex geological processes, such as
 458 wave erosion or tidal influences, could lead to even more realistic
 459 terrains. Additionally, refining the way islands are blended in multi-
 460 island samples, or adding more diverse input conditions (e.g., dif-
 461 ferent geological settings), could help the model generalize better
 462 and produce more varied and dynamic landscapes. While the cur-
 463 rent model allows for rapid terrain generation, adding more options
 464 for users to interact with the cGAN, such as tweaking parameters
 465 like wind strength or island size, could enhance the flexibility of the

- 505 Cordonnier, G., Cani, M.-P., Beneš, B., Braun, J., & Galin, É. 562
 506 (2017). Sculpting mountains: Interactive terrain model- 563
 507 ing based on subsurface geology. *IEEE Transactions on 564*
508 Visualization and Computer Graphics, 24. <https://doi.org/10.1109/TVCG.2017.2689022> (cit. on p. 2). 566
- 510 Cordonnier, G., Galin, É., Gain, J., Beneš, B., Guérin, É., Peytavie, 567
 511 A., & Cani, M.-P. (2017). Authoring landscapes by com- 568
 512 bining ecosystem and terrain erosion simulation. *ACM 569*
513 Transactions on Graphics, 36. <https://doi.org/10.1145/570>
 514 3072959.3073667 (cit. on p. 2). 571
- 515 Dong, C., Loy, C. C., He, K., & Tang, X. (2014). Image super- 572
 516 resolution using deep convolutional networks. <http://arxiv.org/abs/1501.00092> (cit. on p. 8). 574
- 518 Ebert, D. S., Peachey, D., Worley, S., Hart, J. C., Musgrave, K., 575
 519 Perlin, K., & Mark, W. R. (2003). *Texturing and model- 576*
520 ing, a procedural approach (Vol. Third edition). Morgan 577
 521 Kaufmann. (Cit. on p. 2). 578
- 522 Ecormier-Nocca, P., Cordonnier, G., Carrez, P., Moigne, A. M., 579
 523 Memari, P., Benes, B., & Cani, M. P. (2021). Authoring 580
 524 consistent landscapes with flora and fauna. *ACM Trans- 581*
525 actions on Graphics, 40. <https://doi.org/10.1145/582>
 526 3450626.3459952 (cit. on p. 2). 583
- 527 Fournier, A., Fussell, D., & Carpenter, L. (1982). Computer ren- 584
 528 dering of stochastic models. *Communications of the ACM*, 585
 529 25, 371–384. <https://doi.org/10.1145/358523.358553> 586
 530 (cit. on p. 2). 587
- 531 Gain, J., Marais, P., & Straßer, W. (2009). Terrain sketching. *Pro- 588*
532 ceedings of I3D 2009: The 2009 ACM SIGGRAPH Sym- 589
533 posium on Interactive 3D Graphics and Games, 1, 31– 590
 534 38. <https://doi.org/10.1145/1507149.1507155> (cit. on 591
 535 p. 2). 592
- 536 Galin, E., Guérin, E., Peytavie, A., Cordonnier, G., Cani, M.-P., 593
 537 Benes, B., & Gain, J. (2019). A review of digital ter- 594
 538 rain modeling. *Computer Graphics Forum*, 38, 553–577. 595
<https://doi.org/10.1111/cgf.13657> (cit. on p. 2). 596
- 540 Gasch, C., Chover, M., Remolar, I., & Rebollo, C. (2020). Proce- 597
 541 dural modelling of terrains with constraints. *Multimedia 598*
542 Tools and Applications, 79, 31125–31146. <https://doi.org/10.1007/s11042-020-09476-3> (cit. on p. 2). 600
- 544 Gatys, L. A., Ecker, A. S., & Bethge, M. (2015). A neural algorithm 601
 545 of artistic style. <http://arxiv.org/abs/1508.06576> (cit. on 602
 546 p. 8). 603
- 547 Génevaux, J.-D., Galin, É., Peytavie, A., Guérin, É., Briquet, C., 604
 548 Grosbellet, F., & Beneš, B. (2015). Terrain modelling 605
 549 from feature primitives. [https://doi.org/https://doi.org/10.1111/cgf.12530](https://doi.org/10.1111/cgf.12530) (cit. on p. 2). 607
- 551 Guérin, E., Peytavie, A., Masnou, S., Digne, J., Sauvage, B., Gain, 608
 552 J., & Galin, E. (2022). Gradient terrain authoring. *Com- 609*
553 puter Graphics Forum, 41, 85–95. <https://doi.org/10.1111/cgf.14460> (cit. on p. 2). 610
- 555 Guérin, É., Digne, J., Galin, É., & Peytavie, A. (2016). Sparse 612
 556 representation of terrains for procedural modeling. *Com- 613*
557 puter Graphics Forum, 35, 177–187. <https://doi.org/10.1111/cgf.12821> (cit. on p. 8). 614
- 559 Guérin, É., Digne, J., Galin, É., Peytavie, A., Wolf, C., Beneš, 616
 560 B., & Martinez, B. (2017). Interactive example-based 617
 561 terrain authoring with conditional generative adversar- 618
 562 ial networks. *ACM Transactions on Graphics*, 36. <https://doi.org/10.1145/3130800.3130804> (cit. on p. 2).
- Hnaidi, H., Guérin, E., Akkouche, S., Peytavie, A., & Galin, E. (2010). Feature based terrain generation using diffusion equation. *Computer Graphics Forum*, 29, 2179–2186. <https://doi.org/10.1111/j.1467-8659.2010.01806.x> (cit. on p. 2).
- Hopley, D. (2014). *Encyclopedia of modern coral reefs : Structure, form and process*. Springer, Credo Reference. (Cit. on p. 1).
- Isola, P., Zhu, J.-Y., Zhou, T., & Efros, A. A. (2017). Image-to-image translation with conditional adversarial networks. *2017 IEEE Conference on Computer Vision and Pattern Recognition (CVPR)*, 5967–5976. <https://doi.org/10.1109/CVPR.2017.632> (cit. on pp. 1, 2, 6).
- Körner, C., Spehn, E. M., Bugmann, H., & Zurich, E. (2014). *Mountain systems* (tech. rep.). <https://www.researchgate.net/publication/238663492> (cit. on p. 1).
- Lyons, M. B., Murray, N. J., Kennedy, E. V., Kovacs, E. M., Castro-Sanguino, C., Phinn, S. R., Acevedo, R. B., Alvarez, A. O., Say, C., Tudman, P., Markey, K., Roe, M., Canto, R. F., Fox, H. E., Bambic, B., Lieb, Z., Asner, G. P., Martin, P. M., Knapp, D. E., ... Roelfsema, C. M. (2024). New global area estimates for coral reefs from high-resolution mapping. *Cell Reports Sustainability*, 1, 100015. <https://doi.org/10.1016/j.crsus.2024.100015> (cit. on p. 1).
- Mei, X., Decaudin, P., & Hu, B. G. (2007). Fast hydraulic ero- 588
 589 sion simulation and visualization on gpu. *Proceedings - Pacific Conference on Computer Graphics and Applications*, 47–56. <https://doi.org/10.1109/PG.2007.27> (cit. on p. 2).
- Mirza, M., & Osindero, S. (2014). Conditional generative adversarial nets. <http://arxiv.org/abs/1411.1784> (cit. on p. 1).
- Musgrave, F. K., Kolb, C. E., & Mace, R. S. (1989). The synthesis and rendering of eroded fractal terrains. *Proceedings of the 16th Annual Conference on Computer Graphics and Interactive Techniques, SIGGRAPH 1989*, 41–50. <https://doi.org/10.1145/74333.74337> (cit. on p. 2).
- Natali, M., Viola, I., & Patel, D. (2012). Rapid visualization of geological concepts. *Brazilian Symposium of Computer Graphic and Image Processing*, 150–157. <https://doi.org/10.1109/SIBGRAPI.2012.29> (cit. on p. 2).
- Neidhold, B., Wacker, M., & Deussen, O. (2005). Interactive physically based fluid and erosion simulation. *Natural Phenomena*, 25–32. <http://graphics.uni-konstanz.de/publikationen/Neidhold2005InteractivePhysicallyBased/> Neidhold2005InteractivePhysicallyBased.pdf (cit. on p. 2).
- Olsen, J. (2004). Realtime procedural terrain generation. *Department of Mathematics And Computer Science*, 20. <https://pdfs.semanticscholar.org/5961/c577478f21707dad53905362e0ec4e6ec644.pdf> %5Cn<http://www.tsi.enst.fr/~bloch/P6/PRREC/terrain-generation.pdf> %5Cn<http://web.mit.edu/cesium/Public/terrain.pdf> (cit. on p. 2).

- 618 Panagiotou, E., & Charou, E. (2020). Procedural 3d terrain gener- 676
 619 ation using generative adversarial networks. <http://arxiv.org/abs/2010.06411> (cit. on p. 2). 677
 620 Park, J., Redwine, J., Hill, T. D., & Kotun, K. (2019). Water re- 678
 621 source and ecotone transformation in coastal ecosystems. 680
Ecological Modelling, 405, 69–85. <https://doi.org/10.1016/j.ecolmodel.2019.04.015> (cit. on p. 8). 681
 622 Perche, S., Peytavie, A., Benes, B., Galin, E., & Guérin, E. (2023a). 682
 623 Styledem: A versatile model for authoring terrains. <http://arxiv.org/abs/2304.09626> (cit. on p. 8). 683
 624 Perche, S., Peytavie, A., Benes, B., Galin, E., & Guérin, E. 684
 625 (2023b). Authoring terrains with spatialised style. *Computer Graphics Forum*, 42. <https://doi.org/10.1111/cgf.14936> (cit. on p. 8). 685
 626 Perlin, K. (1985). An image synthesizer. *ACM SIGGRAPH Computer Graphics*, 19, 287–296. <https://doi.org/10.1145/325165.325247> (cit. on p. 2). 686
 627 Perlin, K. (2001). Noise hardware. *Real-Time Shading SIGGRAPH Course Notes* (cit. on p. 2). 687
 628 Radford, A., Kim, J. W., Hallacy, C., Ramesh, A., Goh, G., Agar- 688
 629 wal, S., Sastry, G., Askell, A., Mishkin, P., Clark, J., 689
 Krueger, G., & Sutskever, I. (2021). Learning transfer- 690
 630 able visual models from natural language supervision. 691
<http://arxiv.org/abs/2103.00020> (cit. on p. 8). 692
 631 Rombach, R., Blattmann, A., Lorenz, D., Esser, P., & Ommer, B. 693
 632 (2021). High-resolution image synthesis with latent dif- 694
 633 fusion models. <http://arxiv.org/abs/2112.10752> (cit. on 695
 634 p. 8). 696
 635 Schott, H., Paris, A., Fournier, L., Guérin, E., & Galin, E. (2023). 697
 636 Large-scale terrain authoring through interactive erosion 698
 637 simulation. *ACM Transactions on Graphics*, 42, 1–15. 699
<https://doi.org/10.1145/3592787> (cit. on p. 2). 700
 640 Sisodia, Y. (2022). Gan-generated terrain for game assets. *Indian Journal of Artificial Intelligence and Neural Networking*, 2, 1–3. <https://doi.org/10.54105/ijainn.F1060.102622> (cit. on p. 2). 701
 641 Smelik, R. M., Kraker, K. J. D., Groenewegen, S. A., Tutenel, T., 702
 642 & Bidarra, R. (2009). A survey of procedural methods 703
 643 for terrain modelling. *Proceedings of the CASA workshop on 3D advanced media in gaming and simulation (3AMIGAS)* (cit. on p. 2). 704
 644 Spick, R., & Walker, J. A. (2019). Realistic and textured terrain 705
 645 generation using gans. *Proceedings - CVMP 2019: 16th ACM SIGGRAPH European Conference on Visual Media Production*. <https://doi.org/10.1145/3359998.3369407> (cit. on p. 2). 706
 646 Talgorn, F. X., & Belhadj, F. (2018). Real-time sketch-based terrain 707
 647 generation. *ACM International Conference Proceeding Series*, 13–18. <https://doi.org/10.1145/3208159.3208184> (cit. on p. 2). 708
 648 Voulgaris, G., Mademlis, I., & Pitas, I. (2021). Procedural terrain 709
 649 generation using generative adversarial networks. *European Signal Processing Conference, 2021-August*, 686– 710
 650 690. <https://doi.org/10.23919/EUSIPCO54536.2021.9616151> (cit. on p. 2). 711
 651 Wulff-Jensen, A., Rant, N. N., Møller, T. N., & Billeskov, J. A. 712
 652 (2018, January). Deep convolutional generative adversar- 713
 653 ial network for procedural 3d landscape generation based 714
 654 on dem. In *Interactivity, game creation, design, learning, and innovation* (pp. 85–94). Springer. https://doi.org/10.1007/978-3-319-76908-0_9 (cit. on p. 2). 715

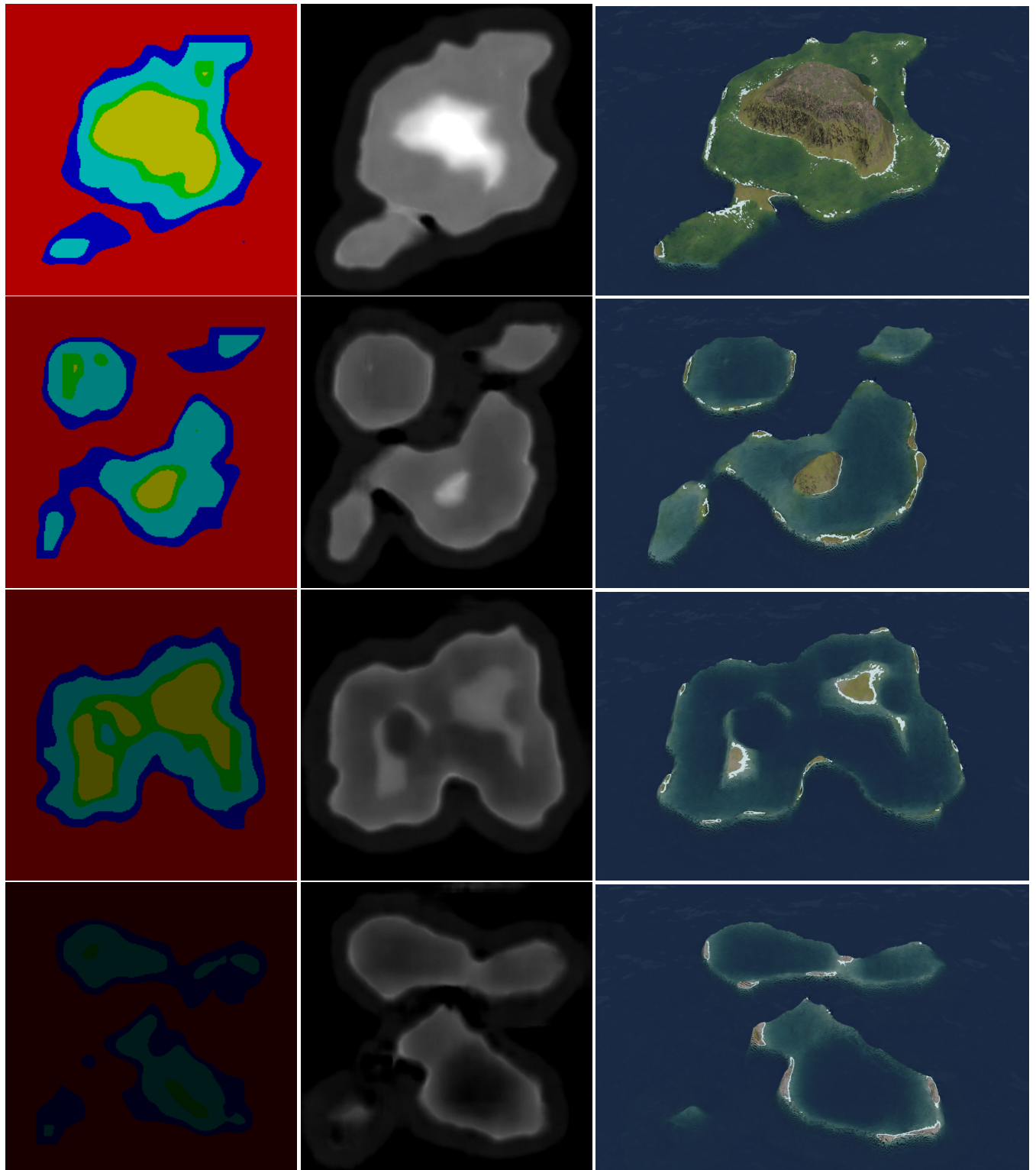


Figure 16: Starting from random Perlin noise, transformed into label maps with increasing subsidence, we can generate a large variety of results.